Article

Representation of a Post-Fire Flash-Flood Event Combining Meteorological Simulations, Remote Sensing, and Hydraulic Modeling

Angelos Alamanos [1], George Papaioannou [2,*], George Varlas [3], Vassiliki Markogianni [3], Anastasios Papadopoulos [3] and Elias Dimitriou [3]

1　Independent Researcher, 10243 Berlin, Germany
2　Department of Forestry and Management of the Environment and Natural Resources, Democritus University of Thrace, 68200 Orestiada, Greece
3　Hellenic Centre for Marine Research, Institute of Marine Biological Resources and Inland Waters, Anavissos, 19013 Athens, Attiki, Greece; gvarlas@hcmr.gr (G.V.); vmarkogianni@hcmr.gr (V.M.); tpapa@hcmr.gr (A.P.); elias@hcmr.gr (E.D.)
*　Correspondence: gpapaio@fmenr.duth.gr

Abstract: Wildfires are an escalating global threat, jeopardizing ecosystems and human activities. Among the repercussions in the ecosystem services of burnt areas, there are altered hydrological processes, which increase the risks of flash floods. There is limited research addressing this issue in a comprehensive way, considering pre- and post-fire conditions to accurately represent flood events. To address this gap, we present a novel approach combining multiple methods and tools for an accurate representation of post-fire floods. The 2019 post-fire flood in Kineta, Central Greece is used as a study example to present our framework. We simulated the meteorological conditions that caused this flood using the atmospheric model WRF-ARW. The burn extent and severity and the flood extent were assessed through remote sensing techniques. The 2D HEC-RAS hydraulic–hydrodynamic model was then applied to represent the flood event, using the rain-on-grid technique. The findings underscore the influence of wildfires on flooding dynamics, highlighting the need for proactive measures to address the increasing risks. The integrated multidisciplinary approach used offers an improved understanding on post-fire flood responses, and also establishes a robust framework, transferable to other similar cases, contributing thus to enhanced flood protection actions in the face of escalating fire-related disasters.

Keywords: burnt areas; flash floods; post-fire flooding; remote sensing; meteorology; hydraulic–hydrodynamic modeling; rain-on-grid; Kineta; Greece

1. Introduction

Wildfires have become an increasingly pressing challenge, with the changing climate exacerbating their extent and severity worldwide [1,2]. This escalating trend threatens ecosystems and human communities, as evidenced by the recurring occurrence of record-high wildfire damages each summer [3]. Countries with drier climates, such as the Mediterranean ones, are particularly susceptible to wildfires, and the summer of 2023 served as compelling evidence [4,5]. This surge in wildfires indicates the need for further research into their hydrological impacts [1], considering the characteristics of the burnt areas.

Wildfires notably alter the vegetation and land cover composition, and soil properties. These fundamental changes directly affect the hydrological behavior of burnt catchments, removing their canopy cover, modifying their runoff patterns, heightening streamflow rates, and increasing sediment transport [6]. Thus, burnt areas are more vulnerable to extreme peak flows [7]. Such effects have been explored from the perspective of identifying the driving factors of post-fire flood risks [8], and the post-fire hazards considering infrastructure sedimentation to hypothetical watersheds [9]. In the context of Mediterranean

regions, where the susceptibility to wildfires is pronounced, studies by Versini et al. [10] and Lavabre et al. [11] have provided valuable insights into the potential hydrological consequences of wildfires, emphasizing the need for region-specific understanding [12,13], including integrated flood risk assessments. Previous works have examined the hydrological response of burnt sites [14], their hydrological and soil-hydraulic properties [15], and the formulation of hydrological models tailored to post-fire runoff simulation [16,17]. Some studies have also analyzed the flood mapping of burnt sites through hydraulic modeling: Godara et al. [18] applied a rain-on-grid technique in the hydraulic model Telemac to explore the response of a Norwegian catchment to a design flood. Theochari and Baltas [19] analyzed the hydrological and hydraulic response of flood-susceptible areas of a burnt site in Evia island, Greece, to a design storm. Furthermore, the effect of flood protection works on flood risk scenarios has been explored for the case of Mandra (Attica, Greece), which is often under wildfire risk [20]. The findings of all these studies converge, demonstrating the large extent of flooded areas following fires that increase the soil imperviousness, increase the peak discharge, and reduce the time to peak of rainfall events [19], and underlining the need for post-fire protection treatments and flood protection works [6,21]. Despite these advancements, a notable gap persists in the literature concerning the response of burnt catchments to real flood events represented by hydraulic models. Existing studies have primarily focused on hypothetical scenarios or design storms. Therefore, understanding the real-world implications of post-fire flood events remains an area in need of comprehensive exploration. There are only a handful of papers studying the response of burnt catchments to real flood events, represented by hydraulic models. This paper aims to fill this gap by simulating a real storm that caused a flash flood in a Greek burnt catchment (Kineta in Central Greece), using meteorological modeling combined with remote sensing techniques for the assessment and validation of fire and flood events, and mapping the flood with hydraulic–hydrodynamic modeling, for the first time to our knowledge.

The simulation of the exact meteorological conditions of the event was conducted using the Advanced Weather and Research Forecasting (WRF-ARW) model. This enables the precise representation of the flood event under real storm conditions [22,23]. The atmospheric model WRF-ARW has been used to simulate various meteorological conditions in Greece, demonstrating a satisfactory level of performance under different tests [24]. Furthermore, it has successfully simulated heavy precipitation events resulting in flash floods [25], and predicted extreme storms [26] and flood events [22]. Although rainfall inputs from WRF-ARW have been coupled with land hydrological models before [27], this is, to our knowledge, the first application where the WRF-ARW weather model inputs are used directly for hydraulic modeling, exploiting the rain-on-grid technique of HEC-RAS [28]. This is a fundamental difference compared to the sole closest previous application that our team employed for a different site [29], as the rain-on-grid allows a higher level of spatial resolution, reflecting the actual rainfall patterns and variability across the study area.

Another challenge in flood simulation studies is the accurate knowledge of the flooded areas, and additionally in our case, considering a post-fire flood, the accurate knowledge of the burnt area. New technologies such as remote sensing (RS) have been successfully used to provide detailed information on burn extent and severity [30–33], as well as flooded areas [34–36]. In this work, we leverage the use of RS to assess both the burn extent and severity, and the flooded parts of the study area. Burn severity and extent are critical factors that directly influence post-fire land use changes in the catchment, while knowledge of the flooded area is essential for developing an accurate hydraulic model and validating it.

Overall, this study introduces a novel, integrated, and multidisciplinary framework for accurately assessing post-fire flood events. It combines different methodological approaches, uses new modeling tools, and is easily transferable to other cases, offering thus an improved understanding of the impacts of combined fire–flood disasters.

2. Study Area

The Kineta catchment, covering approximately 40 km^2, is located in western Attica. Its northern part drains the Geraneia mountains towards its southern part, through the Pikas and two other, smaller, intermittent streams, where the coastal town of Kineta is located (Figure 1). Part of the Geraneia mountains is a Natura 2000 Protected Area. The climate is a typical Mediterranean climate, with hot, dry summers and mild, wet winters [37].
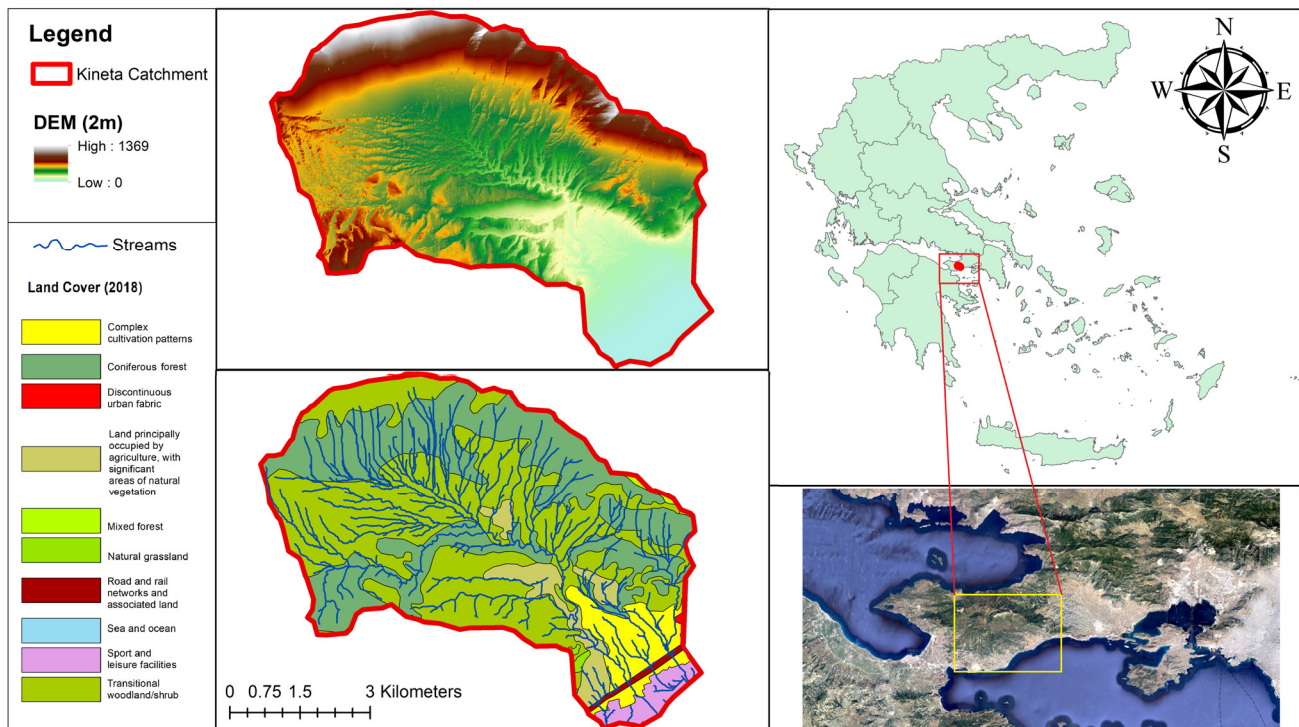

Figure 1. The map of the study area, showing the location of Kineta in Greece and the catchment with the digital elevation model (DEM) [38], the river network, and the pre-fire land cover in 2018 according to the CORINE classification [39].

The wider Kineta area has suffered in the past from flood events, with some incidents reported in 1961 and 1977, with limited information available [40]. In September 2018, the storm 'Zorbas' caused increased streamflows in the stream Pikas [41], and the main roads above the town of Kineta were temporarily closed for precautionary reasons [42].

The Kineta area, a typical Greek site facing multiple interconnected water-related challenges [43], has also suffered from wildfires, with notable incidents in 2017 and 2018 (Figure 2). On May 14, 2017, a fire broke out in the Panorama settlement in Agioi Theodoroi, Corinthia (northwest of Kineta), claiming two lives and causing two injuries. The fire reached close to the area's settlements and consumed one of them [44].

On July 23, 2018, a large fire ravaged the pine forest of the Geraneia Mountains above Kineta. The fire was attributed to strong winds bringing power lines into contact, causing sparks that resulted in the ignition of dry grass [45], while there were also debates regarding the possibility of an organized arson [46]. The fire advanced and burned down the Panorama and Galini settlements, as well as houses in Kineta, causing 14 injuries.

Figure 2. (**A**) Damage caused by the fire of 2017. Source: [44]. (**B**) The burnt pine forest after the fire of 2018. Source: [47]. (**C**,**D**) Damage caused by the fire of 2018. Source: [48].

The next year (2019), an extreme storm event, named 'Girionis' by meteorologists, took place between November 24 and November 26 and caused a destructive flash flood [49]. Among the findings of the subsequent visual inspection, it was found that the fire of 2018 played a key role in the magnitude of the flood damages [47]. After the fires in 2018, an inspection revealed that there were already loose sediments in significant quantities within the riverbeds [47]. The flood brought downstream a considerable amount of sediment (mud, trees, rocks, etc.), which, combined with the large volume of water, caused severe damages, as will be shown later.

However, there has been no comprehensive, data-driven assessment so far investigating the mechanisms involved and under which this flood occurred. In particular, we examine whether Girionis was such an extreme phenomenon that it was mainly responsible for the flood, or to what extent Kineta faced the consequences of the partial recovery of forest, land cover, and vegetation restoration, as well as the streams blocked by sediments.

In the following sections, we describe the process followed for the simulation of the Girionis storm and Kineta's hydraulic response to the post-fire flash flood of 2019.

3. Materials and Methods

Here, each sub-section presents each main modeling step. In particular, the atmospheric model is presented first, which allowed us to accurately simulate the exact meteorological conditions that led to the 2019 flood in Kineta. The results of our meteorologic model consist of the rain-on-grid technique's inputs to the hydraulic model. The burn extent and severity and the actual flood extent were assessed using RS. This allowed us to obtain detailed information on the spatial distribution of burned areas, helping us to understand post-fire land use changes, which change the roughness coefficients of the hydraulic model. Additionally, it provided critical data on the flooded regions, essential for validating and refining the hydraulic model. The hydraulic model simulates the flood event, where the inclusion of the rain-on-grid technique allowed for a higher spatial resolution, reflecting actual rainfall patterns and variability across the study area, along with a detailed analysis of flood dynamics, considering the altered hydrological processes due to

the wildfire. The integration of meteorological modeling, RS, and hydraulic–hydrodynamic modeling facilitated a comprehensive analysis of the complex post-fire flooding conditions.

3.1. Simulating the Storm That Caused the Flood

The Advanced Weather and Research Forecasting (WRF-ARW) v4.2 model [50] was used to simulate the meteorological conditions resulting in the heavy precipitation event that caused the flash flood in Kineta. The WRF-ARW model is one the most used limited-area numerical weather prediction models, and is capable of simulating adverse weather conditions such as cyclones and severe storms [51]. A significant advantage of the WRF-ARW model is its physics-based representation of complex processes during storms (e.g., convection, cloud microphysics, turbulence), which thus facilitates a detailed and accurate forecasting of the amount and spatiotemporal distribution of heavy rainfall. The model was set up by adopting a similar methodology as for the flash flood that occurred in the neighboring region of Mandra, Attica, Greece on 15 November 2017, which is presented in detail in Papaioannou et al. [52]. The model here was set up on three nested domains with horizontal grid spacings of 9 km × 9 km (644 × 360 grid points), 3 km × 3 km (292 × 286 grid points), and 1 km × 1 km (187 × 154 grid points), respectively. The third domain well covered the flooded area and some adjacent regions, the second domain covered Greece, and the first one covered a wide area including parts of Europe, the Mediterranean, North Africa, and West Asia, respectively. The simulation was initialized on 24 November at 00:00 GMT (02:00 local time) to capture the atmospheric conditions prior to the flash flood, and the simulation lasted 48 h, up to 26 November at 00:00 GMT (02:00 local time). The initial and boundary (every 6 h) conditions of the simulation were constructed using operational analysis data of the Global Forecasting System (GFS), provided by the National Centers for Environmental Prediction (NCEP), on a horizontal grid spacing of 0.25° × 0.25°. The initial conditions involved atmospheric data at several atmospheric layers and near the surface, as well as soil moisture and temperature. The sea surface temperature (SST) measurements in the lower boundary conditions of the simulation were updated every 6 h and they were constructed using real-time global (RTG) SST analysis data, also provided by the NCEP, on a horizontal grid spacing of 0.083° × 0.083°. The ground processes were parameterized employing the unified Noah [53] land surface model. The long-wave and short-wave radiation processes were parameterized using the RRTMG scheme [54]. Also, the WSM 5-class scheme [55] was used to parameterize the cloud microphysics processes. Regarding the convective processes, the Grell–Freitas ensemble scheme [56] was employed in the calculations of the first domain (9 km × 9 km), while explicit resolve of convection was used in the second and third domains (3 km × 3 km and 1 km × 1 km). Moreover, the Yonsei University scheme (YSU) [57] and the revised Monin–Obukhov scheme were employed for the planetary boundary layer and the surface layer processes, respectively.

3.2. Assessing the Characteristics of Kineta's Burnt Area and Mapping of Burn Severity

Three Sentinel 2 satellite imageries of pre-fire (1 image) and post-fire (2 images) were used for the mapping of the burnt area of the Kineta area, after the fire of 23 July 2018. Sentinel 2A Level 1C tiles (tile ID: T34SFH) were acquired on 20 July 2018 (before the fire event), 02 August 2018 (after the fire event), and 16 October 2019 (before the flood event under investigation), and downloaded from the Copernicus Open Access Hub [58]. The selection of the Sentinel 2 imagery was based on the tiling grid, which is available via the ESA [59] as a KML file, providing unique IDs for each tile (100 km × 100 km ortho-images in UTM/WGS84 projection).

Followingly, Sentinel 2 images were pre-processed by being imported in the semi-automatic classification plugin (SCP) of the free and open-source cross-platform desktop Quantum Geographic Information System (Q-GIS), v. 3.6.3-Noosa, to perform: (a) a conversion of the images from digital numbers (DNs) to top-of-atmosphere reflectance

(TOA), and (b) atmospheric correction (AC) by using the DOS1 method (an AC method widely used by the Earth Observation community [60,61]).

The study area was delineated by using the shapefile of the Kineta catchment including adjacent watersheds, while the mapping of burnt areas has been conducted for two periods; the first one concerns the period between July and August 2018, and the second one concerns the period between July 2018 and October 2019 with a basic aim of the detection of regrown vegetation.

Burnt areas were mapped based on the double calculation of Normalized Burn Ratio (*NBR*) (Equation (1)) [62] for both periods, by using bands B08 (NIR) and B12 (SWIR). This index uses the differences of reflected light between healthy and burnt vegetation based on the fact that green vegetation presents a very high reflectance in the NIR and a low reflectance in the SWIR portion of the spectrum, while recently burnt areas present low reflectance in the NIR and high reflectance in the SWIR [63]. The *NBR* index takes values ranging from −1 to +1, with the healthy green and burnt vegetation presenting high and low values, respectively.

$$NBR = \frac{(\text{NIR} - \text{SWIR})}{(\text{NIR} + \text{SWIR})} \tag{1}$$

Subsequently, the change in Normalized Burn Ratio (delta *NBR—dNBR*) [62] was twofold calculated to highlight the changes from the reference state, by subtracting the post-fire *NBR* values (2 August 2018 and 16 October 2019) from the reference *NBR* value of 20 July 2018 (Equation (2)). In this way, burn severity is more accurately assessed than through the *NBR* index, as it is based on the measurement of per-pixel changes in reflectance values.

$$dNBR = NBR\,prefire - NBR\,postfire \tag{2}$$

Followingly, according to Rahman et al. [64], a threshold value of +0.1 (proposed for Sentinel 2 images) was set to both *dNBR* files for each period to appropriately differentiate the burnt areas from unburnt areas along the study area.

Conclusively, the resulting *dNBR* values were multiplied by 1000 and afterwards classified according to burn severity ranges proposed by the United States Geological Survey (USGS) (Figure 3). Two-fold calculation of the *dNBR* highlighted initially the most affected-by-wildfire areas for each period and then the observed changes in burn severity levels from August 2018 to October 2019.

	Severity Level	dNBR Range (scaled by 10^3)	dNBR Range (not scaled)
	Enhanced Regrowth, high (post-fire)	-500 to -251	-0.500 to -0.251
	Enhanced Regrowth, low (post-fire)	-250 to -101	-0.250 to -0.101
	Unburned	-100 to +99	-0.100 to +0.99
	Low Severity	+100 to +269	+0.100 to +0.269
	Moderate-low Severity	+270 to +439	+0.270 to +0.439
	Miderate-high Severity	+440 to +659	+0.440 to +0.659
	High Severity	+660 to +1300	+0.660 to +1.300

Figure 3. Burn severity levels of Kineta, proposed by the relevant USGS Table.

3.3. Delineation of Flood-Inundated Areas

Most attempts to map flood-inundated areas through remote sensing data utilize either spectral data from optical sensors or backscatter data from synthetic aperture radar (SAR) imagery [65]. Although SAR imagery is capable of penetrating darkness and cloudiness, it is affected by noise-like speckle and the inability to differentiate water and water-like surfaces [66,67]. Additionally, Konapala et al. [66] explored the use of S2 bands (through water indices) and S1 SAR imagery concerning their capability for generating accurate flood inundation maps, while their results indicated the statistically significant superiority of S2 band-based indices compared to the respective S1. Based initially on those results and then on the fact that the only appropriate and available S1 SAR image of Kineta catchment was of 27 November 2019, one cloud-free Sentinel 2 (S2) image of 25 November 2019 with

the processing level 1C and time 09:23:21:024Z was used to map flood-inundated areas in Kineta after the flood event that started on 24 November 2019. The S2 image was subjected to the same pre-processing procedures as those used for the mapping of burnt areas.

Concerning the delineation of water on land, spectral indices containing visual bands with a wavelength (μm) between 0.5 and 0.7 and near-infrared spectra with a wavelength (μm) of 0.7 to 1.1 have been proven the most successful [68,69]. Therefore, in this study, several spectral indices (NDWI, MNDWI, AWEI, RSWIR1, and RSWIR2) have been evaluated by employing S2 bands.

In addition to these spectral indices, the SWIR2, NIR, and red bands were ascribed to Red, Green, and Blue values (RGB), respectively, and converted to the HSV (Hue, Saturation, Value) colors using a standardized transformation [70]. According to Pekel et al. [71,72], water can be effectively delineated by defining a relation between the H, S, and V components, while more information about the theoretical background and the equations used can be found in Konapala et al. [66].

Five water indices (WIs) were calculated on the S2 image of 25 November 2019 (Figure 4), while the most significant task was to select the most representative threshold value for each WI. Analysis of their histograms indicates a different magnitude peak, while positive indices' values normally correspond to water while negative or zero values correspond to soil or terrestrial vegetation. In addition, manual (subjective) adjustment of the thresholds is proven to achieve a more accurate result in the water delineation, which was performed based on the actual images (pictures) and drone videos from the visual inspection after the flood [39,62]. Then, after the application of the thresholds, each image file representing each distinct WI was binarized, inputting a logical value (true) for values greater than the threshold and a false value for lower values. The process for deciding which 'water' image best describes the flooded area will be discussed in Section 4.2.
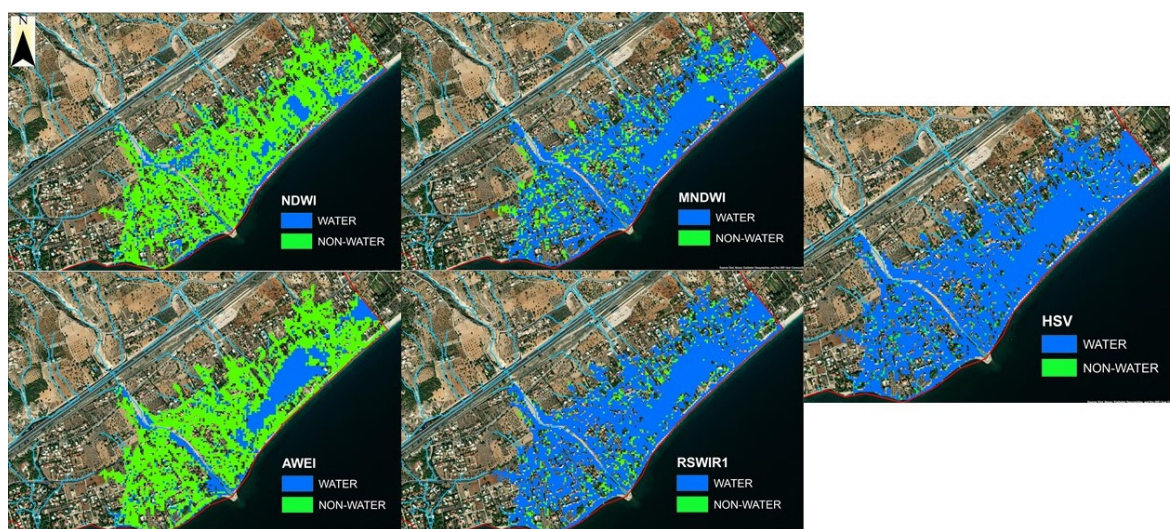

Figure 4. Binarized spatial maps of calculated WIs.

3.4. Simulating the Flood Event

The hydraulic–hydrodynamic modeling has been conducted using the 2D Hydrologic Engineering Center's River Analysis System (HEC-RAS) to map the inundated areas of the studied catchment, and analyze the water depth and velocity during the studied event. The main components needed for precise flood inundation modeling and mapping include the digital elevation model (DEM), stream channel characteristics (such as river flowpaths and banks), the hydraulic model setup (including initial and boundary conditions, roughness coefficients, and engineering structures), as well as the depiction of urban areas [73–75]. A 2 m resolution DEM was applied in this case, obtained from the National Cadastre and Mapping Agency S.A. (NCMA) [38].

Roughness is a key input in flood inundation modeling, as it directly affects the flow conditions. The most common approach for the reasonable mapping of the Manning's roughness coefficients (n) is the use of typical values for land cover data based on the literature, combined with personal judgment based on the area's characteristics. This approach was followed in this case, combining CORINE land cover data and typical values for pre- and post-fire land use categories, always considering the burn severity conditions. The spatially distributed roughness values used for the Kineta area were derived after testing considering the typical minimum, median, and maximum n values provided by the literature for similar areas and conditions (in particular: [17,76–85]), aiming for the optimum set of values.

The 2D hydrodynamic calculations were based on a computational grid covering the study area, using a variable high-resolution mesh computation point. The small mesh spacing, especially around streams, makes the computations more demanding, but ensures a high level of modeling detail.

The rain-on-grid technique was used, allowing us to spatially apply the detailed rainfall accompanying the storm that caused the flood event, as simulated by the WRF-ARW atmospheric model, on a grid over the Kineta catchment. The time step of the rain-on-grid storm applied was 1 h, so 20 spatial datasets (raster files—20 grids from 24 November 2019 14:00:00 to 25 November 2019 09:00:00) representing the storm event were inserted in HEC-RAS. The simulation was configured based on these inputs, as follows: the computation interval was set to 1 s, while the mapping, the hydrograph, and the detailed output intervals were set to 5 min.

For the validation of the model, the flooded area's polygon as obtained from the RS imagery was used and assessed with typical indices that consider the flood extent. In particular, the Critical Success Index (CSI), also known as threat score (TS) was used to assess the accuracy of the simulated inundated areas against the validation polygon [86–88]. The CSI can be estimated according to Equation (3):

$$\text{CSI} = \frac{A}{A + B + C} \tag{3}$$

where *A* is the correctly simulated flooded area (hits); *B* is the false-simulated flooded area (false alarms); *C* is the flooded area that is not predicted by the model (misses); and the term *B* at the numerator in Equation (3) is used to penalize the model's overprediction [89,90].

4. Results and Discussion

4.1. Meteorological Analysis of the Flash Flood Event

On 24–25 November, Greece was affected by severe weather conditions. A deep barometric low from the west brought heavy precipitation in many areas. More specifically, a cold front, accompanying the barometric low, passed through the night between 24 and 25 November causing torrential rainfall in Kineta and adjacent areas. A meteorological station of the National Observatory of Athens (NOA) network at Agioi Theodoroi located approximately 8 km west–southwest of Kineta recorded 206.8 mm of 2-day rainfall on 24–25 November (daily data available from 'meteo'—a Greek weather portal [91]). This precipitation amount is extreme if one considers that the annual precipitation at this area is about 400–450 mm [92]. The WRF-ARW model simulation estimated 182.6 mm of 2-day rainfall at the same area, thus agreeing very well with the measurements. The results of the WRF-ARW model, namely the simulated storm of the 24–25 November, are shown in Figure 5. Most of the rain was simulated from 24 November at 20:00 GMT (22:00 local time) to 25 November at 06:00 GMT (08:00 local time), as shown in Figure 5a. Especially in the early morning of 25 November, a severe storm occurred around Kineta, as indicated by the pattern and intensity of the 1 h accumulated precipitation in Figure 5b–d for 03:00, 04:00, 05:00, and 06:00 local time, respectively. The storm developed south–southwest of Kineta, and then it gradually moved towards the Kineta area. The precipitation maps highlight the persistence of the storm in the Kineta area compared to adjacent areas. The high rainfall

rates caused significant increases in surface water runoff in the watershed upstream of Kineta, finally resulting in the devastating flash flood. It is important to note here that there were no reports of major hydroclimatic events in this area from the time of fire to the time of flood, implying that the combination of severe rainfall with burnt area might be the only two factors triggering this flash flood event.

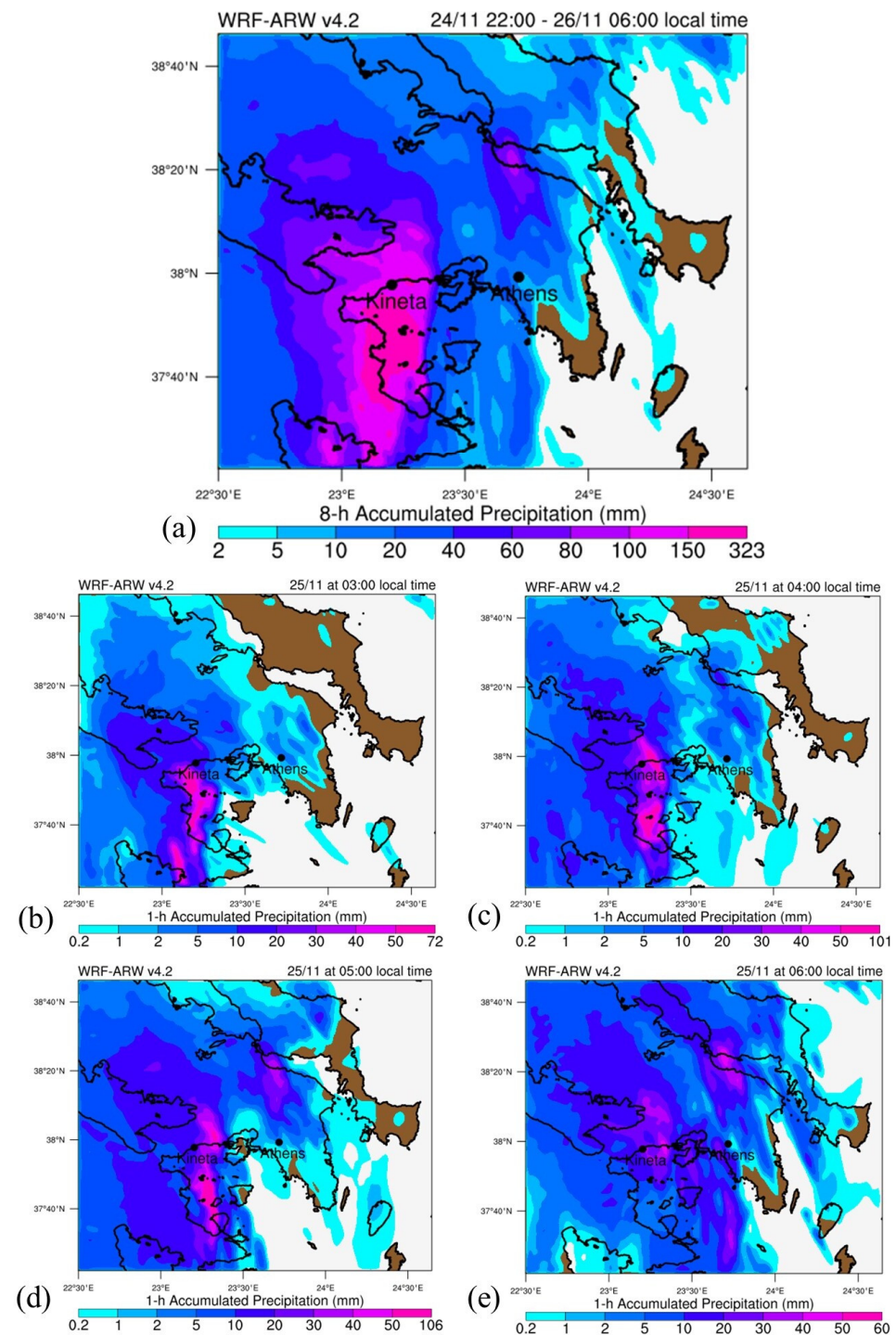**Figure 5.** (**a**) Simulated 8 h accumulated precipitation (mm) for the period from 24 November at 20:00 GMT (22:00 local time) to 25 November at 06:00 local time. Simulated 1 h accumulated precipitation (mm) for 25 November at (**b**) 01:00, (**c**) 02:00, (**d**) 03:00, and (**e**) 04:00 GMT (03:00–06:00 local time). The figures show the storm progression over the greater Kineta-Athens area.

4.2. Analysis of Wildfire Damages and Flood Extent Mapping

For both periods (July–August 2018 and July 2018–October 2019), the burn severity classes covering the greatest areas are those subjected to moderate–high and moderate–low severity and the unburnt areas (2018), and moderate–low and low severity and unburnt areas for October 2019, respectively. It should also be noted that areas affected by high burn severity in October 2019 are almost minimized compared to August of 2018 and are mainly replaced by areas impacted by moderate–low burn severity (Figure 6).
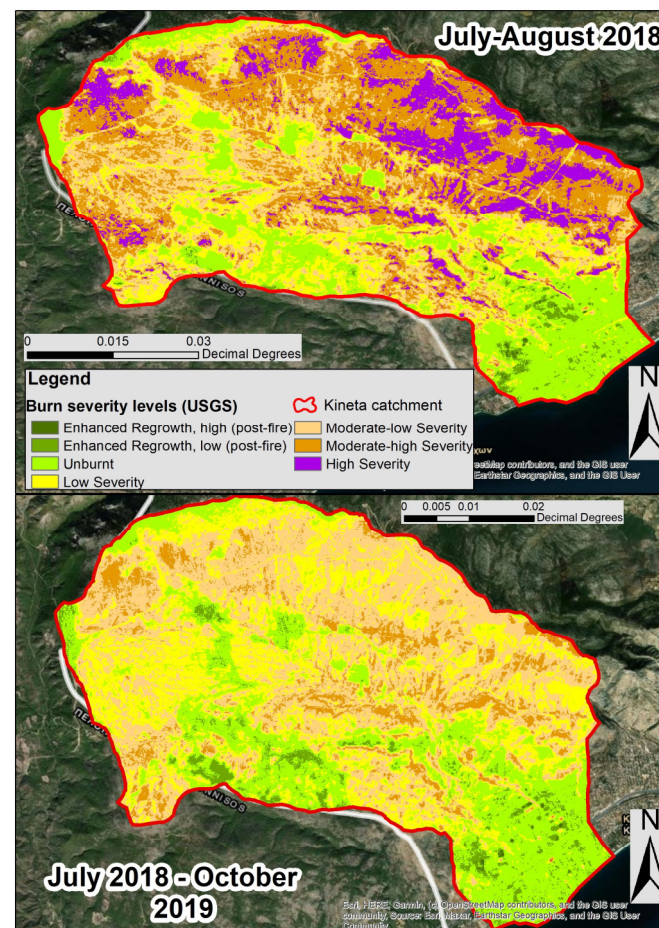

Figure 6. Burn severity maps.

The two-fold calculation and the comparison of the degree of fire-induced changes between the studied periods indicated a reduction in the fire's effect over time and across certain areas. Sentinel's high spatial resolution offered the potential to improve the ecological interpretation of heterogeneous burn severity effects and managed to detect the vegetation regrowth, the increased moisture, and the decreased exposure of ash between August 2018 and October 2019.

For the mapping of the flood extent, all calculated WIs were compared, interpreted by using expert knowledge and visually checked, aligned to the 4 (Red)-3 (Green)-2 (Blue) natural composite of the respective S2 image. Intensified analysis highlighted the RSWIR2 (accompanied by the threshold value ≥ -0.1) as the best performing index for the detection of inundated areas (Figure 7), as it presented the most stable results.
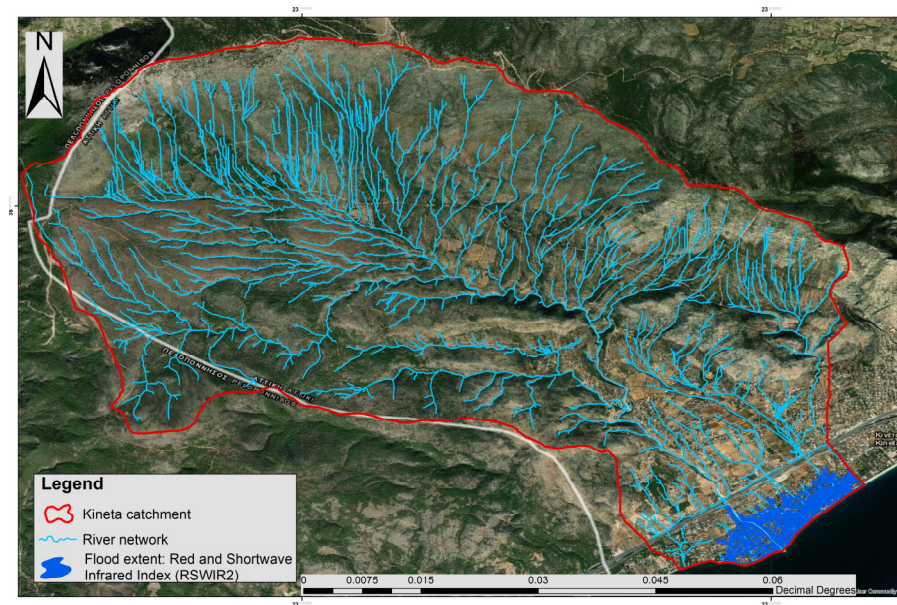
Figure 7. Flood extent mapped through RSWIR2 index calculation.

It is also worth noting that during the period of July 2018–November 2019, the land use did not change in the studied catchment [39,93]. The mountainous northern part consists of the forest, and the 'middle' part of the catchment has various vegetation classes, which, as we go to the southern part, gives way to grassland and crops, until the coastal town of Kineta [93].

4.3. Hydraulic–Hydrodynamic Modeling Results

After the tests were performed, two set of values of the n roughness coefficient were defined (Table 1). These values were used in a spatially distributed format for the Kineta area and combined with the DEM, the 2D flow area computational grid, and the rain-on-grid input constituting the model setup for the initial (pre-fire) and the post-fire conditions, respectively. In Table 1, the Classification Category field corresponds to the CORINE 2018 land cover categories (CLC2018), combined with the different conditions derived from the RS observations (RS obs). So, the CLC2018 categories (e.g., complex cultivation patterns, coniferous forest, mixed forest, etc.) were spatially combined with the RS observations (e.g., enhanced regrowth high, enhanced regrowth low, high severity, low severity, moderate–low severity, moderate–high severity, unburnt), and produced the categories of the first column of Table 1. This actually shows us spatially all the different land cover categories (according to CORINE) with their different burn/recovered status (based on the RS observations).

Table 1. Manning's roughness n values for the pre-fire and pos-fire scenario. The post-fire scenario corresponds to the actual simulated flood of November 2019.

Classification Category (CLC2018 and RS obs)	Manning's n (Pre-Fire Scenario)	Manning's n (Post-Fire Scenario)
Complex cultivation patterns, enhanced regrowth, high (post fire)	0.650	0.4903
Complex cultivation patterns, enhanced regrowth, low (post fire)	0.650	0.1708
Complex cultivation patterns, high severity	0.650	0.0110
Complex cultivation patterns, low severity	0.650	0.4903
Complex cultivation patterns, moderate–low severity	0.650	0.3305
Complex cultivation patterns, moderate–high severity	0.650	0.1708
Complex cultivation patterns, unburnt	0.650	0.6500
Coniferous forest, enhanced regrowth, high (post fire)	0.800	0.6028
Coniferous forest, enhanced regrowth, low (post fire)	0.800	0.2083
Coniferous forest, high severity	0.800	0.0110

Table 1. *Cont.*

Classification Category (CLC2018 and RS obs)	Manning's n (Pre-Fire Scenario)	Manning's n (Post-Fire Scenario)
Coniferous forest, low severity	0.800	0.6028
Coniferous forest, moderate–low severity	0.800	0.4055
Coniferous forest, moderate–high severity	0.800	0.2083
Coniferous forest, unburnt	0.800	0.8000
Discontinuous urban fabric, enhanced regrowth, low (post fire)	0.060	0.0233
Discontinuous urban fabric, low severity	0.060	0.0478
Discontinuous urban fabric, moderate–low severity	0.060	0.0355
Discontinuous urban fabric, unburnt	0.060	0.0600
Land principally occupied by agriculture with significant areas of natural vegetation enhanced regrowth, high (post fire)	0.050	0.0403
Land principally occupied by agriculture with significant areas of natural vegetation enhanced regrowth, low (post fire)	0.050	0.0208
Land principally occupied by agriculture with significant areas of natural vegetation, low severity	0.050	0.0403
Land principally occupied by agriculture with significant areas of natural vegetation, moderate–low severity	0.050	0.0305
Land principally occupied by agriculture with significant areas of natural vegetation, moderate–high severity	0.050	0.0208
Land principally occupied by agriculture with significant areas of natural vegetation, unburnt	0.050	0.0500
Mixed forest, enhanced regrowth, low (post fire)	0.800	0.2083
Mixed forest, high severity	0.800	0.0110
Mixed forest, low severity	0.800	0.6028
Mixed forest, moderate–low severity	0.800	0.4055
Mixed forest, moderate–high severity	0.800	0.2083
Mixed forest, unburnt	0.800	0.8000
Natural grassland, enhanced regrowth, high (post fire)	0.650	0.4903
Natural grassland, enhanced regrowth, low (post fire)	0.650	0.1708
Natural grassland, low severity	0.650	0.4903
Natural grassland, moderate–low severity	0.650	0.3305
Natural grassland, unburnt	0.650	0.6500
Road and rail networks and associated land, enhanced regrowth, high (post fire)	0.013	0.0130
Road and rail networks and associated land, enhanced regrowth, low (post fire)	0.013	0.0130
Road and rail networks and associated land, low severity	0.013	0.0130
Road and rail networks and associated land, unburnt	0.013	0.0130
Sea and ocean, enhanced regrowth, high (post fire)	0.070	0.0700
Sea and ocean, enhanced regrowth, low (post fire)	0.070	0.0700
Sea and ocean, low severity	0.070	0.0700
Sea and ocean, unburnt	0.070	0.0700
Sport and leisure facilities, enhanced regrowth, high (post fire)	0.025	0.0215
Sport and leisure facilities, enhanced regrowth, low (post fire)	0.025	0.0145
Sport and leisure facilities, high severity	0.025	0.0110
Sport and leisure facilities, low severity	0.025	0.0215
Sport and leisure facilities, moderate–low severity	0.025	0.0180
Sport and leisure facilities, moderate–high severity	0.025	0.0145
Sport and leisure facilities, unburnt	0.025	0.0250
Transitional woodland/shrub, enhanced regrowth, high (post fire)	0.800	0.6028
Transitional woodland/shrub, enhanced regrowth, low (post fire)	0.800	0.2083
Transitional woodland/shrub, high severity	0.800	0.0110
Transitional woodland/shrub, low severity	0.800	0.6028
Transitional woodland/shrub, moderate–low severity	0.800	0.4055
Transitional woodland/shrub, moderate–high severity	0.800	0.2083
Transitional woodland/shrub, unburnt	0.800	0.8000
Streams	0.060	0.0950

Moreover, the hydraulic model considered the information retrieved from the visual inspection after the fire of 2018 and the flood of November 2019, as reported in the respective report, the news, and a drone video of the flooded area (as shown in Figure 8). This allowed us to:

1. Create an accurate representation of the validation polygon of the areas that flooded within the town of Kineta by refining the RS results of Figure 7 according to the relevant descriptions and photos. This improved, 'modified' validation polygon is shown in Figure 8, along with the relevant photos and references.
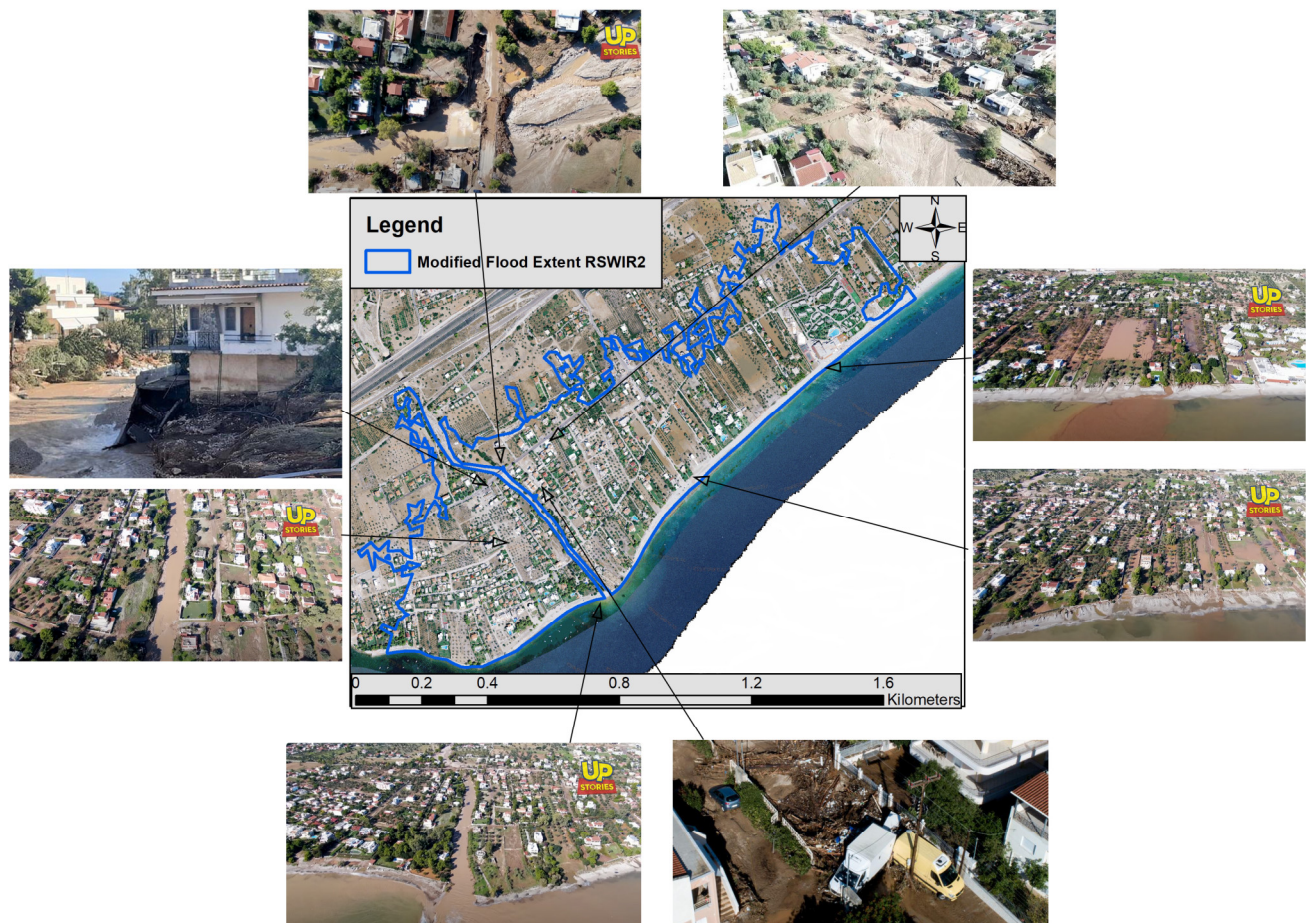

Figure 8. The actual flood extent, as extracted from the RS observations of Figure 7, and refined with the documented damages after the visual inspection of the flood event of November 2019 [47], sourced from the Greek news [94] and a drone video taken by the UPstories team showing the aftermath of the flood [95].

2. Consider the effect of the debris flow to the blocked drainage routes. In particular, after the fire, it was reported that a considerable amount of rocks, mud, and wood mass blocked the Pika stream's drainage passage before the Olympia highway, and an underground culvert at the two other smaller streams in the east (Figure 9). Figures and further details justifying this can be found in the visual inspection report [47]. These were not blocked under the initial (pre-fire) conditions, so the hydraulic model took into account these changes:

    ○   In the pre-fire conditions, the Pika stream is considered to be a typical-surface, open stream, while the other two streams have an orthogonal culvert of 3×5 m for water drainage to the sea.

○ In the post-fire conditions, these are blocked, so the Pika stream was blocked above the Olympia highway (using HEC-RAS's terrain modification toolbox), and the culvert is inactive.
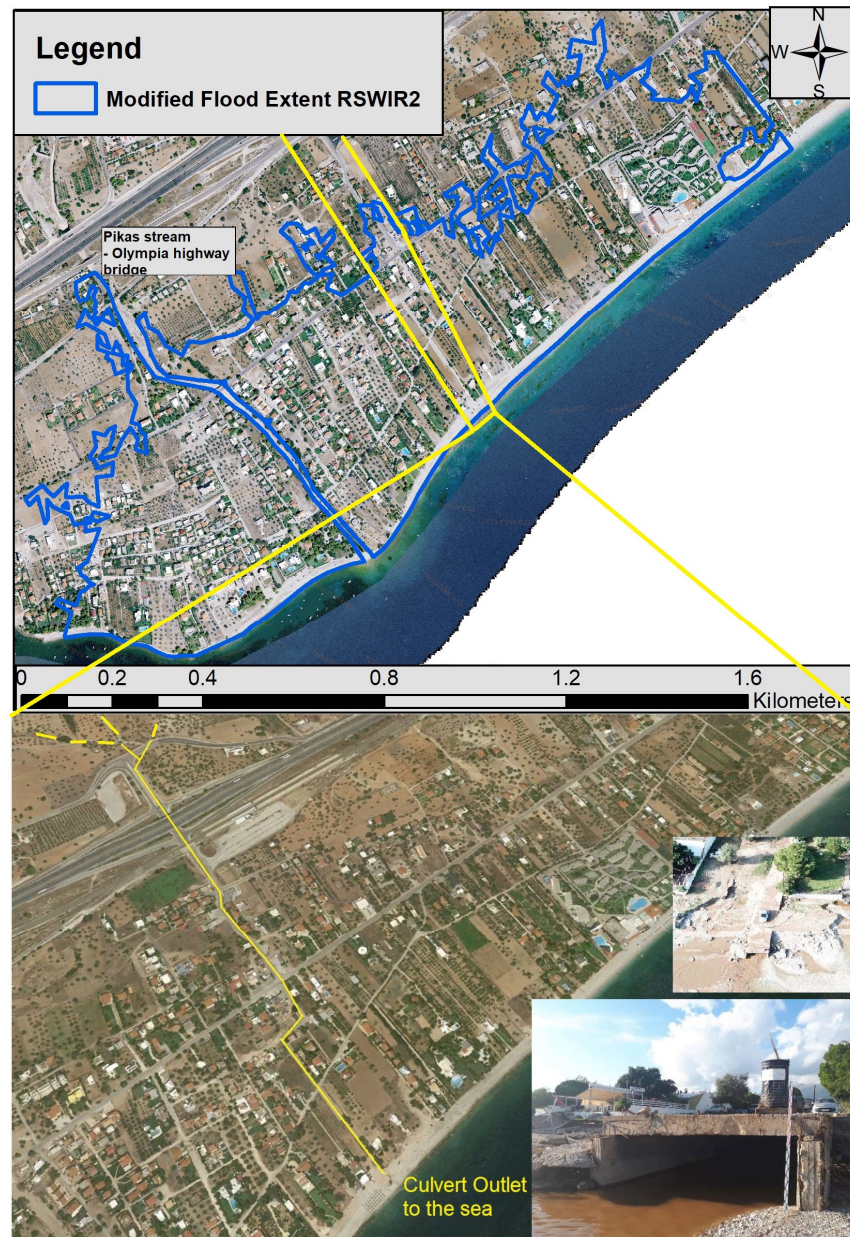

Figure 9. The location of the Pika stream–Olympia highway bridge (Athens–Corinth route); in the second picture, there is a schematic of the underground culvert until its outlet to the sea. The post-fire flood of November 2019 blocked both drainage routes. Sources: Google Earth; [47,94,95].

In these views from Figures 8 and 9, it is worth noting how many houses have been built close to the streams, maximizing thus their exposure risks from potential damages of a flood event.

The results of the hydraulic–hydrodynamic simulations are shown in Figure 10, considering the baseline (pre-fire) initial conditions, and the actual conditions of the 2019 flood (post-fire scenario).
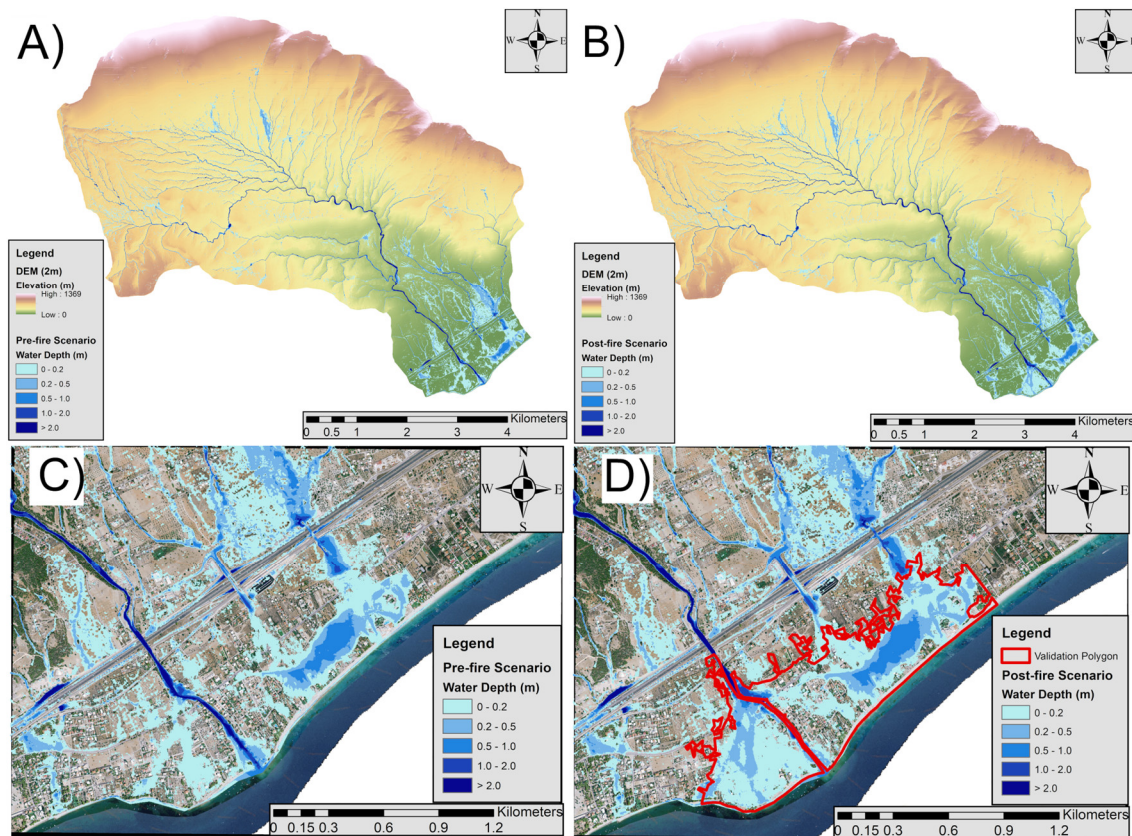
Figure 10. The results of the hydraulic–hydrodynamic model under the Girionis storm: (**A**) Flood extent for the initial pre-fire conditions; (**B**) Flood extent for the real post-fire conditions, representing the flood event of November 2019. Both scenarios' simulations were run with the rain-on-grid technique. The flood depth results for the Kineta town area in comparison with the validation polygon (of Figure 8) are shown in figures: (**C**) for the pre-fire conditions, and (**D**) for the post-fire conditions.

The validation of the hydraulic model's results was performed based the CSI scores, as described in Section 3.4 (Equation (3)). The CSI for the flood of November 2019 in Kineta was 0.65, which is a satisfactory value (CSIs above 0.5 are acceptable).

The total simulated flood inundation area was found to be 451,848 m^2 (411,177 m^2 inside the validation polygon) for the pre-fire scenario, and 595,246 m^2 (549,308 m^2 inside the validation polygon) for the post-fire scenario. So, the actual effect of the fire on the flood extent is 143,398 m^2 more flooding in total, with the 138,131 m^2 within the validation polygon. This practically proves that if the Kineta pine forest had not been burned, and the streams were not then blocked, the flood extent would have been reduced by 25.1%. At the catchment scale, this might sound a small difference; however, for a small coastal town covering approximately 4.5 km^2, the 0.138 km^2 is not negligible.

Figure 11 illustrates this difference between the flood extents between the pre-fire and the post-fire scenarios for the town of Kineta (the difference between Figure 10C,D, within the validation polygon area). The major difference is observed in the southwest where most of the Pikas stream overflows were routed. However, both banks of Pikas stream were affected by the post-fire conditions. Other minor effects are observed in the northern part of the city, where the other two smaller streams exhibited slightly increased flows. The effect of the blocked culverts is obvious. With respect to the water depth, the overall differences are small, at the scale of 0–0.2 m, but the flooding extent had the biggest difference. Again, it is worth noting that several houses are located very close to all three streams' banks.
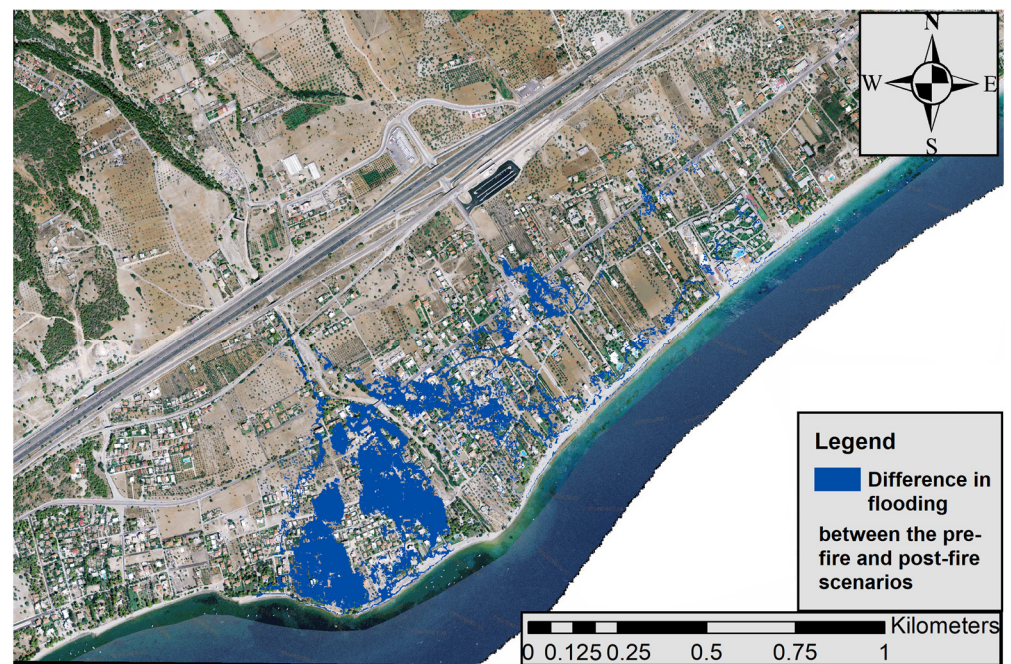
Figure 11. The effect of the wildfire on the additional flood inundation within the Kineta town, compared to the pre-fire scenario.

In any case, as mentioned in the results in Section 3.1, the Girionis storm was indeed a severe phenomenon. This indicates a potential flood risk in the area, regardless of the fire, as the hydraulic model's results confirmed for the initial pre-fire conditions (especially in the eastern part of Kineta). This finding is in line with some other historic flood events, as mentioned in the study area section. Moreover, the results of the RS analysis (Section 3.2) showed that the land cover and vegetation have recovered from August 2018 since October 2019, although not completely, but the high-burn severity areas were minimized.

An interesting finding is that the Pikas stream was not the only one responsible for the flood. A considerable amount of water also came from the other two smaller streams in the eastern part of the catchment, mainly the one in the east. These are intermittent streams, but it seems that their more abrupt slopes contributed to their increased streamflows. Another factor that contributed to the increased post-fire flood scenario was the streams being blocked by the flow of debris.

5. Conclusions

In this study, a new, integrated framework was introduced for the accurate representation of flood events based on real conditions. Its strength lies on the combination of different methodological approaches (atmospheric, RS, hydraulic modeling) that can also be applied to other case studies allowing the detailed assessment of post-fire flood disasters.

The atmospheric model WRF-ARW allowed us to represent the exact meteorological conditions that caused the flood, thus making available the key input forcing (rainfall) for the hydraulic model HEC-RAS. The rain-on-grid technique was found to be particularly useful for this kind of analysis, as it enables the application of the simulated storm rainfall on a grid. Another element that contributed to the level of detail of this analysis was the DEM resolution being 2 m. The contribution of the RS input was also crucial and necessary for the accurate setup of the hydraulic model based on the land cover changes due to the fire (post-fire conditions) and the validation of the flood inundation mapping, based on the actual flood that was observed.

The 2019 flood in Kineta was simulated for the first time, offering a thorough view of the event and its implications, and the actual effect of the fire. During the period between the wildfire and the flood, no other significant change to the study area was observed, e.g.,

any major land use change, a long-term drought, or any extreme precipitation event. Our results showed that although the storm was severe and there would have been a flood anyway, the partial recovery of the land cover and the vegetation of the burnt site, along with the flow streams being blocked by debris, contributed to the flood extent increasing by 25.1%, which is non-negligible for a small town.

Thus, one would wonder if the post-fire flood was an unavoidable phenomenon or if there could have been any potential actions and protection measures in place to prevent it. Our results underscore the need for at least considering such protection measures, aiming to mitigate such risks. The most common ways to achieve this is by applying post-fire soil erosion and flood protection treatments [6], which can: (i) 'cut' the extreme streamflow from the channels using check dams or other barriers; (ii) maintain and clean certain drainage flowpaths; and (iii) boost the recovery of the land cover, the vegetation, and the soil, speeding up the recovery of burnt sites, enhancing the water retention potential, and improving their hydrological response to extreme events. Future research could consider finding where there should be soil erosion and flood protection treatments and examining their potential performance under these real conditions. We believe that it is crucial to assess (and even quantify) the contribution of such protection measures to achieve a potentially reduced flood extent, and to assess to what degree this could be achieved. The results of this work showed that the post-fire conditions resulted in a 25.1% increased flood extent compared to the pre-fire conditions, which indicates the need for post-fire flood protection techniques that apparently were not in place. Moreover, the finding that the two smaller streams of the area contribute to the flooding with significant amounts of water (even in the pre-fire scenario) indicates the need for flood protection measures, including floodplain zones, targeting these areas.

In general, it is difficult to estimate or predict the effects of a fire on the hydrological response of a catchment, as these can be very case-specific and highly dependent on various factors. The presented approach can be applied to other catchments as a methodological framework, and is expected to be particularly useful for Mediterranean regions facing increasing fire and flood risks. Thus, it can contribute to an improved understanding of such risks and strengthen protection efforts with more informed decisions.

Data Availability Statement: Data available on request. The data are not publicly available due to [The data are not publicly available due to to restrictions imposed by the providing local authorities, limiting their use solely for our designated research purposes].

Conflicts of Interest: The authors declare no conflicts of interest.

References

1. Time to Recover. *Nat. Sustain.* **2023**, *6*, 1027. [CrossRef]
2. Alamanos, A.; Koundouri, P. *Emerging Challenges and the Future of Water Resources Management*; Hydrolink 2022/10; International Association for Hydro-Environment Engineering and Research (IAHR): Madrid, Spain, 2022. Available online: https://henry.baw.de/items/148979b1-38fa-4211-962c-f046a86bd13e (accessed on 8 November 2023).
3. Duane, A.; Castellnou, M.; Brotons, L. Towards a Comprehensive Look at Global Drivers of Novel Extreme Wildfire Events. *Clim. Chang.* **2021**, *165*, 43. [CrossRef]
4. Papagiannaki, K.; Giannaros, T.M.; Lykoudis, S.; Kotroni, V.; Lagouvardos, K. Weather-Related Thresholds for Wildfire Danger in a Mediterranean Region: The Case of Greece. *Agric. For. Meteorol.* **2020**, *291*, 108076. [CrossRef]
5. Ruffault, J.; Curt, T.; Moron, V.; Trigo, R.M.; Mouillot, F.; Koutsias, N.; Pimont, F.; Martin-StPaul, N.; Barbero, R.; Dupuy, J.-L.; et al. Increased Likelihood of Heat-Induced Large Wildfires in the Mediterranean Basin. *Sci. Rep.* **2020**, *10*, 13790. [CrossRef] [PubMed]
6. Papaioannou, G.; Alamanos, A.; Maris, F. Evaluating Post-Fire Erosion and Flood Protection Techniques: A Narrative Review of Applications. *GeoHazards* **2023**, *4*, 380–405. [CrossRef]

7. Liu, M.; Wei, H.; Dong, X.; Wang, X.-C.; Zhao, B.; Zhang, Y. Integrating Land Use, Ecosystem Service, and Human Well-Being: A Systematic Review. *Sustainability* **2022**, *14*, 6926. [CrossRef]

8. Yilmaz, O.S.; Akyuz, D.E.; Aksel, M.; Dikici, M.; Akgul, M.A.; Yagci, O.; Balik Sanli, F.; Aksoy, H. Evaluation of Pre- and Post-Fire Flood Risk by Analytical Hierarchy Process Method: A Case Study for the 2021 Wildfires in Bodrum, Turkey. *Landsc. Ecol. Eng.* **2023**, *19*, 271–288. [CrossRef]

9. Jong-Levinger, A.; Banerjee, T.; Houston, D.; Sanders, B.F. Compound Post-Fire Flood Hazards Considering Infrastructure Sedimentation. *Earth's Future* **2022**, *10*, e2022EF002670. [CrossRef]

10. Versini, P.-A.; Velasco, M.; Cabello, A.; Sempere-Torres, D. Hydrological Impact of Forest Fires and Climate Change in a Mediterranean Basin. *Nat. Hazards* **2013**, *66*, 609–628. [CrossRef]

11. Lavabre, J.; Torres, D.S.; Cernesson, F. Changes in the Hydrological Response of a Small Mediterranean Basin a Year after a Wildfire. *J. Hydrol.* **1993**, *142*, 273–299. [CrossRef]

12. Coscarelli, R.; Aguilar, E.; Petrucci, O.; Vicente-Serrano, S.M.; Zimbo, F. The Potential Role of Climate Indices to Explain Floods, Mass-Movement Events and Wildfires in Southern Italy. *Climate* **2021**, *9*, 156. [CrossRef]

13. Shah, S.A.; Jehanzaib, M.; Park, K.W.; Choi, S.; Kim, T.-W. Evaluation and Decomposition of Factors Responsible for Alteration in Streamflow in Lower Watersheds of the Han River Basin Using Different Budyko-Based Functions. *KSCE J. Civ. Eng.* **2023**, *27*, 903–914. [CrossRef]

14. Folador, L.; Cislaghi, A.; Vacchiano, G.; Masseroni, D. Integrating Remote and In-Situ Data to Assess the Hydrological Response of a Post-Fire Watershed. *Hydrology* **2021**, *8*, 169. [CrossRef]

15. Ebel, B.A.; Moody, J.A. Parameter Estimation for Multiple Post-Wildfire Hydrologic Models. *Hydrol. Process.* **2020**, *34*, 4049–4066. [CrossRef]

16. Wang, J.; Stern, M.A.; King, V.M.; Alpers, C.N.; Quinn, N.W.T.; Flint, A.L.; Flint, L.E. PFHydro: A New Watershed-Scale Model for Post-Fire Runoff Simulation. *Environ. Model. Softw.* **2020**, *123*, 104555. [CrossRef]

17. Ebel, B.A.; Shephard, Z.M.; Walvoord, M.A.; Murphy, S.F.; Partridge, T.F.; Perkins, K.S. Modeling Post-Wildfire Hydrologic Response: Review and Future Directions for Applications of Physically Based Distributed Simulation. *Earth's Future* **2023**, *11*, e2022EF003038. [CrossRef]

18. Godara, N.; Bruland, O.; Alfredsen, K. Simulation of Flash Flood Peaks in a Small and Steep Catchment Using Rain-on-Grid Technique. *J. Flood Risk Manag.* **2023**, *16*, e12898. [CrossRef]

19. Theochari, A.-P.; Baltas, E. Holistic Hydrological Approach to the Fire Event on August 2021 in Evia, Greece. *Euro-Mediterr J. Environ. Integr.* **2022**, *7*, 287–298. [CrossRef]

20. Mitsopoulos, G.; Diakakis, M.; Panagiotatou, E.; Sant, V.; Bloutsos, A.; Lekkas, E.; Baltas, E.; Stamou, A.I. 'How Would an Extreme Flood Have Behaved If Flood Protection Works Were Built?' The Case of the Disastrous Flash Flood of November 2017 in Mandra, Attica, Greece. *Urban Water J.* **2022**, *19*, 911–921. [CrossRef]

21. Mitsopoulos, G.; Diakakis, M.; Bloutsos, A.; Lekkas, E.; Baltas, E.; Stamou, A. The Effect of Flood Protection Works on Flood Risk. *Water* **2022**, *14*, 3936. [CrossRef]

22. Zhou, J.; Zhang, H.; Zhang, J.; Zeng, X.; Ye, L.; Liu, Y.; Tayyab, M.; Chen, Y. WRF Model for Precipitation Simulation and Its Application in Real-Time Flood Forecasting in the Jinshajiang River Basin, China. *Meteorol. Atmos. Phys.* **2018**, *130*, 635–647. [CrossRef]

23. Alamanos, A.; Linnane, S. Drought monitoring, precipitation statistics, and water balance with freely available remote sensing data: Examples, advances, and limitations. In Proceedings of the Irish National Hydrology Conference 2021, Athlone, Ireland, 16 November 2021; pp. 1–13.

24. Emmanouil, G.; Vlachogiannis, D.; Sfetsos, A. Exploring the Ability of the WRF-ARW Atmospheric Model to Simulate Different Meteorological Conditions in Greece. *Atmos. Res.* **2021**, *247*, 105226. [CrossRef]

25. Toros, H.; Kahraman, A.; Tilev-Tanriover, S.; Geertsema, G.; Cats, G. Simulating Heavy Precipitation with HARMONIE, HIRLAM and WRF-ARW: A Flash Flood Case Study in İstanbul, Turkey. *EJOSAT* **2018**, *Volume 13*, 1–12. [CrossRef]

26. Patel, P.; Ghosh, S.; Kaginalkar, A.; Islam, S.; Karmakar, S. Performance Evaluation of WRF for Extreme Flood Forecasts in a Coastal Urban Environment. *Atmos. Res.* **2019**, *223*, 39–48. [CrossRef]

27. Junior, J.; Oliveira, V.D.P.; Sales, D. Rainfall input from WRF-ARW Atmospheric Model coupled with MOHID Land Hydrological Model for flow simulation in the Paraíba Do Sul River–Brazil. *J. Urban Environ. Eng.* **2021**, *15*, 188–203. [CrossRef]

28. Hydrologic Engineering Center (HEC). *River Analysis Systems—HEC-RAS, version 6.3.1*; U.S. Army Corps of Engineers: Washington, DC, USA, 2022.

29. Papaioannou, G.; Varlas, G.; Terti, G.; Papadopoulos, A.; Loukas, A.; Panagopoulos, Y.; Dimitriou, E. Flood Inundation Mapping at Ungauged Basins Using Coupled Hydrometeorological–Hydraulic Modelling: The Catastrophic Case of the 2006 Flash Flood in Volos City, Greece. *Water* **2019**, *11*, 2328. [CrossRef]

30. Gibson, R.; Danaher, T.; Hehir, W.; Collins, L. A Remote Sensing Approach to Mapping Fire Severity in South-Eastern Australia Using Sentinel 2 and Random Forest. *Remote Sens. Environ.* **2020**, *240*, 111702. [CrossRef]

31. Gibson, R.K.; Mitchell, A.; Chang, H.-C. Image Texture Analysis Enhances Classification of Fire Extent and Severity Using Sentinel 1 and 2 Satellite Imagery. *Remote Sens.* **2023**, *15*, 3512. [CrossRef]

32. Quintano, C.; Fernández-Manso, A.; Fernández-Manso, O. Combination of Landsat and Sentinel-2 MSI Data for Initial Assessing of Burn Severity. *Int. J. Appl. Earth Obs. Geoinf.* **2018**, *64*, 221–225. [CrossRef]

33. García-Llamas, P.; Suárez-Seoane, S.; Fernández-Guisuraga, J.M.; Fernández-García, V.; Fernández-Manso, A.; Quintano, C.; Taboada, A.; Marcos, E.; Calvo, L. Evaluation and Comparison of Landsat 8, Sentinel-2 and Deimos-1 Remote Sensing Indices for Assessing Burn Severity in Mediterranean Fire-Prone Ecosystems. *Int. J. Appl. Earth Obs. Geoinf.* **2019**, *80*, 137–144. [CrossRef]

34. Shen, X.; Wang, D.; Mao, K.; Anagnostou, E.; Hong, Y. Inundation Extent Mapping by Synthetic Aperture Radar: A Review. *Remote Sens.* **2019**, *11*, 879. [CrossRef]

35. Bhattacharya, B.; Mazzoleni, M.; Ugay, R. Flood Inundation Mapping of the Sparsely Gauged Large-Scale Brahmaputra Basin Using Remote Sensing Products. *Remote Sens.* **2019**, *11*, 501. [CrossRef]

36. Lin, Y.; Wang, J.; Yue, M. Equity-Based Grid Resilience: How Do We Get There? *Electr. J.* **2022**, *35*, 107135. [CrossRef]

37. Filis, C.; Spyrou, N.I.; Diakakis, M.; Kotroni, V.; Lagouvardos, K.; Papagiannaki, K.; Vassilakis, E.; Milios, D.; Lekkas, E. Post-Wildfire Flash Flooding in Small Mountainous Catchments: Post-Fire Effects and Characteristics of the November 2019 Flash Flood in Kineta, Greece, EGU General Assembly 2020, Online, 4–8 May 2020, EGU2020-5501. 2020. Available online: https://meetingorganizer.copernicus.org/EGU2020/EGU2020-5501.html (accessed on 8 November 2023).

38. National Cadastre and Mapping Agency, S.A. —Organizations—GEODATA.Gov.Gr. Available online: https://geodata.gov.gr/en/organization/ekxa (accessed on 7 December 2023).

39. CORINE Land Cover 2018 (Vector/Raster 100 m), Europe, 6-Yearly. Available online: https://land.copernicus.eu/en/products/corine-land-cover/clc2018 (accessed on 7 December 2023).

40. Petrou, A.; Moustris, J. November is the month with the most flood victims in Attica. *Meteo.gr*–Προγνώσεις καιρού για όλη την Ελλάδα. 2022. (In Greek). Available online: https://www.meteo.gr/article_view.cfm?entryID=810 (accessed on 8 November 2023).

41. LoutrakiNews. Kineta: Post-Fire Floods—High Streamflows in Pikas Stream. (In Greek). Available online: https://www.loutraki365.gr/blog/post/kineta-meta-tis-pyrkagies-oi-plimmyres-terasties-posotites-neroy-sto-rema-tis-pikas (accessed on 8 November 2023).

42. Ta Nea. Zorbas Storm Hits Attica—Closed Roads. (In Greek). Available online: https://www.tanea.gr/2018/09/30/greece/o-zormpas-xtypise-kai-tin-attiki-xaos-stous-dromous-apo-tis-plimmyres/ (accessed on 8 November 2023).

43. Angeli, A.; Karkani, E.; Alamanos, A.; Xenarios, S.; Mylopoulos, N. Hydrological, socioeconomic, engineering and water quality modeling aspects for evaluating water security: Experience from Greek Rural Watersheds. In Proceedings of the EGU General Assembly, Online, 4–8 May 2020; EGU: Vienna, Austria, 2020.

44. Mononews. New updates from Kineta: One dead from the fire, two injured and one missing. *Mononews.gr*. 2017. (In Greek). Available online: https://www.mononews.gr/politics/news-politiki-megali-pirkagia-stin-kineta-fotia-kaei-konta-se-spitia (accessed on 8 November 2023).

45. Eleftheros typos. The fire in Kineta started from the electricity piles—Details of the report. *Eleftheros Typos*. 2019. (In Greek). Available online: https://www.panhellenicpost.com/2018/09/14/%CE%B1%CF%80%CF%8C-%CE%BA%CE%B1%CE%BB%CF%8E%CE%B4%CE%B9%CE%B1-%CF%84%CE%B7%CF%82-%CE%B4%CE%B5%CE%B7-%CE%B7-%CF%86%CF%89%CF%84%CE%B9%CE%AC-%CF%83%CF%84%CE%B7%CE%BD-%CE%BA%CE%B9%CE%BD%CE%AD%CF%84%CE%B1/ (accessed on 8 November 2023).

46. Souliotis, G. The mistakes started from Kineta. *Kathimerini*. 2019. (In Greek). Available online: https://www.kathimerini.gr/society/1031440/apo-tin-kineta-xekinisan-ta-lathi/ (accessed on 8 November 2023).

47. Lekkas, E.; Spyrou, N.; Filis, C.; Diakakis, M.; Vassilakis, E.; Katsetsiadou, A.; Milios, D.; Arianoutsou, M.; Faragitakis, G.; Christopoulou, A.; et al. *The November 25, 2019 Kineta (Western Attica) Flood*; Athens, Greece, 2019; (In Greek). Available online: https://www.newsit.gr/uncategorized/etsi-pnigike-i-kineta-aytopsia-tou-kathigiti-eythymiou-lekka-pics/2922935/ (accessed on 8 November 2023).

48. Vimaonline. Kineta is a barren land after the fire—The fire was rekindled. *Vimaonline*. (In Greek). Available online: https://www.vimaonline.gr/20/article/33316/kraniou-topos-i-kineta-apo-tin-purkagia-anazopurothike-i-fotia (accessed on 8 November 2023).

49. Protothema. Storm "Girionis": How Kineta was burned—Visual inspection in the area. *ProtoThema*. 2019. (In Greek). Available online: https://www.protothema.gr/webtv/default-folder/3715449/kakokairia-giryonis-pws-i-pyrkagia-epnikse-tin-kineta/ (accessed on 8 November 2023).

50. Skamarock, C.; Klemp, B.; Dudhia, J.; Gill, O.; Liu, Z.; Berner, J.; Wang, W.; Powers, G.; Duda, G.; Barker, D.; et al. *A Description of the Advanced Research WRF Model Version 4.3*; OpenSky: Boulder, CO, USA, 2021. [CrossRef]

51. Varlas, G.; Pytharoulis, I.; Steeneveld, G.-J.; Katsafados, P.; Papadopoulos, A. Investigating the Impact of Sea Surface Temperature on the Development of the Mediterranean Tropical-like Cyclone "Ianos" in 2020. *Atmos. Res.* **2023**, *291*, 106827. [CrossRef]

52. Papaioannou, G.; Varlas, G.; Papadopoulos, A.; Loukas, A.; Katsafados, P.; Dimitriou, E. Investigating Sea-State Effects on Flash Flood Hydrograph and Inundation Forecasting. *Hydrol. Process.* **2021**, *35*, e14151. [CrossRef]

53. Tewari, M.; Boulder, C.; Chen, F.; Wang, W.; Dudhia, J.; LeMone, M.; Mitchell, K.; Ek, M.; Gayno, G.; Wegiel, J.; et al. Implementation and Verification of the Unified Noah Land Surface Model in the WRF Model. In Proceedings of the 20th Conference on Weather Analysis and Forecasting/16th Conference on Numerical Weather Prediction, Seattle, WA, USA, 14 January 2004. Volume Formerly Paper Number 17.5.

54. Iacono, M.J.; Delamere, J.S.; Mlawer, E.J.; Shephard, M.W.; Clough, S.A.; Collins, W.D. Radiative Forcing by Long-Lived Greenhouse Gases: Calculations with the AER Radiative Transfer Models. *J. Geophys. Res. Atmos.* **2008**, *113*, D13103. [CrossRef]

55. Hong, S.-Y.; Dudhia, J.; Chen, S.-H. A Revised Approach to Ice Microphysical Processes for the Bulk Parameterization of Clouds and Precipitation. *Mon. Weather. Rev.* **2004**, *132*, 103–120. [CrossRef]
56. Grell, G.A.; Freitas, S.R. A Scale and Aerosol Aware Stochastic Convective Parameterization for Weather and Air Quality Modeling. *Atmos. Chem. Phys.* **2014**, *14*, 5233–5250. [CrossRef]
57. Hong, S.-Y.; Noh, Y.; Dudhia, J. A New Vertical Diffusion Package with an Explicit Treatment of Entrainment Processes. *Mon. Weather. Rev.* **2006**, *134*, 2318–2341. [CrossRef]
58. Copernicus. The Sentinels Scientific Data Hub. Available online: https://scihub.copernicus.eu/maintenance.html#/home (accessed on 2 February 2023).
59. Sentinel Datasets. Sentinel-2—Data Products—Sentinel Handbook. Available online: https://copernicus.eu/missions/sentinel-2/data-products (accessed on 2 November 2023).
60. Barrett, D.C.; Frazier, A.E. Automated Method for Monitoring Water Quality Using Landsat Imagery. *Water* **2016**, *8*, 257. [CrossRef]
61. Japitana, M.V.; Demetillo, A.T.; Burce, M.E.C.; Taboada, E.B. Catchment Characterization to Support Water Monitoring and Management Decisions Using Remote Sensing. *Sustain. Environ. Res.* **2019**, *29*, 8. [CrossRef]
62. Key, C.; Benson, N. *Landscape Assessment (LA)*; USDA Forest Service, Rocky Mountain Research Station: Ogden, UT, USA, 2006.
63. Petropoulos, G.P.; Griffiths, H.M.; Kalivas, D.P. Quantifying Spatial and Temporal Vegetation Recovery Dynamics Following a Wildfire Event in a Mediterranean Landscape Using EO Data and GIS. *Appl. Geogr.* **2014**, *50*, 120–131. [CrossRef]
64. Rahman, S.; Chang, H.-C.; Hehir, W.; Magilli, C.; Tomkins, K. Inter-Comparison of Fire Severity Indices from Moderate (Modis) and Moderate-To-High Spatial Resolution (Landsat 8 & Sentinel-2A) Satellite Sensors. In Proceedings of the IGARSS 2018–2018 IEEE International Geoscience and Remote Sensing Symposium, Valencia, Spain, 22–27 July 2018; pp. 2873–2876.
65. Shen, X.; Anagnostou, E.N.; Allen, G.H.; Robert Brakenridge, G.; Kettner, A.J. Near-Real-Time Non-Obstructed Flood Inundation Mapping Using Synthetic Aperture Radar. *Remote Sens. Environ.* **2019**, *221*, 302–315. [CrossRef]
66. Konapala, G.; Kumar, S.V.; Khalique Ahmad, S. Exploring Sentinel-1 and Sentinel-2 Diversity for Flood Inundation Mapping Using Deep Learning. *ISPRS J. Photogramm. Remote Sens.* **2021**, *180*, 163–173. [CrossRef]
67. Alsdorf, D.E.; Rodríguez, E.; Lettenmaier, D.P. Measuring Surface Water from Space. *Rev. Geophys.* **2007**, *45*, 1–24. [CrossRef]
68. Boschetti, M.; Nutini, F.; Manfron, G.; Brivio, P.A.; Nelson, A. Comparative Analysis of Normalised Difference Spectral Indices Derived from MODIS for Detecting Surface Water in Flooded Rice Cropping Systems. *PLoS ONE* **2014**, *9*, e88741. [CrossRef] [PubMed]
69. Memon, A.A.; Muhammad, S.; Rahman, S.; Haq, M. Flood Monitoring and Damage Assessment Using Water Indices: A Case Study of Pakistan Flood-2012. *Egypt. J. Remote Sens. Space Sci.* **2015**, *18*, 99–106. [CrossRef]
70. Smith, A.R. Color Gamut Transform Pairs. In Proceedings of the 5th Annual Conference on Computer Graphics and Interactive Techniques, New York, NY, USA, 23 August 1978; Association for Computing Machinery: New York, NY, USA; pp. 12–19.
71. Pekel, J.-F.; Vancutsem, C.; Bastin, L.; Clerici, M.; Vanbogaert, E.; Bartholomé, E.; Defourny, P. A near Real-Time Water Surface Detection Method Based on HSV Transformation of MODIS Multi-Spectral Time Series Data. *Remote Sens. Environ.* **2014**, *140*, 704–716. [CrossRef]
72. Pekel, J.-F.; Cottam, A.; Gorelick, N.; Belward, A.S. High-Resolution Mapping of Global Surface Water and Its Long-Term Changes. *Nature* **2016**, *540*, 418–422. [CrossRef] [PubMed]
73. Xu, H. Modification of Normalised Difference Water Index (NDWI) to Enhance Open Water Features in Remotely Sensed Imagery. *Int. J. Remote Sens.* **2006**, *27*, 3025–3033. [CrossRef]
74. Papaioannou, G.; Vasiliades, L.; Loukas, A.; Alamanos, A.; Efstratiadis, A.; Koukouvinos, A.; Tsoukalas, I.; Kossieris, P. A Flood Inundation Modeling Approach for Urban and Rural Areas in Lake and Large-Scale River Basins. *Water* **2021**, *13*, 1264. [CrossRef]
75. Leitão, J.P.; de Sousa, L.M. Towards the Optimal Fusion of High-Resolution Digital Elevation Models for Detailed Urban Flood Assessment. *J. Hydrol.* **2018**, *561*, 651–661. [CrossRef]
76. Kalyanapu, A.; Burian, S.; McPherson, T. Effect of Land Use-Based Surface Roughness on Hydrologic Model Output. *J. Spat. Hydrol.* **2009**, *9*, 51–71.
77. Weltz, M.A.; Arslan, A.B.; Lane, L.J. Hydraulic Roughness Coefficients for Native Rangelands. *J. Irrig. Drain. Eng.* **1992**, *118*, 776–790. [CrossRef]
78. Moore, D.; Todea, N.; Cerrelli, G.; Yochum, S.; Norman, J.; Hoeft, C. *Hydrologic Analyses of Post-Wildfire Conditions*; Natural Resources Conservation Service, U.S. Department of Agriculture: Washington, DC, USA, 2016; p. 146.
79. Canfield, H.E.; Goodrich, D. *Suggested Changes to AGWA to Account for Fire (V 2.1)*; USDA-ARS Southwest Watershed Research Center: Tucson, AZ, USA, 2005. Available online: https://directives.sc.egov.usda.gov/OpenNonWebContent.aspx?content=39877.wba (accessed on 8 November 2023).
80. Canfield, H.E.; Goodrich, D.C.; Burns, I.S. Selection of parameters values to model post-fire runoff and sediment transport at the watershed scale in southwestern forests. In *Managing Watersheds for Human and Natural Impacts: Engineering, Ecological, and Economic Challenges*; American Society of Civil Engineers: Reston, VA, USA, 2012; pp. 1–12. [CrossRef]
81. Lefrancq, M.; Van Dijk, P.; Jetten, V.; Schwob, M.; Payraudeau, S. Improving Runoff Prediction Using Agronomical Information in a Cropped, Loess Covered Catchment. *Hydrol. Process.* **2017**, *31*, 1408–1423. [CrossRef]

82. Sanz-Ramos, M.; Bladé, E.; González-Escalona, F.; Olivares, G.; Aragón-Hernández, J.L. Interpreting the Manning Roughness Coefficient in Overland Flow Simulations with Coupled Hydrological-Hydraulic Distributed Models. *Water* **2021**, *13*, 3433. [CrossRef]

83. Senarath, S.U.S.; Ogden, F.L.; Downer, C.W.; Sharif, H.O. On the Calibration and Verification of Two-Dimensional, Distributed, Hortonian, Continuous Watershed Models. *Water Resour. Res.* **2000**, *36*, 1495–1510. [CrossRef]

84. Pradhan, N.R.; Floyd, I. Event Based Post-Fire Hydrological Modeling of the Upper Arroyo Seco Watershed in Southern California. *Water* **2021**, *13*, 2303. [CrossRef]

85. Alamanos, A.; Papaioannou, G. Developing a Hydrological Model for Grand River Watershed, Ontario. In Proceedings of the 3rd IAHR Young Professionals Congress, IAHR, Online, 22 November 2022.

86. Di Baldassarre, G.; Schumann, G.; Bates, P.D.; Freer, J.E.; Beven, K.J. Flood-Plain Mapping: A Critical Discussion of Deterministic and Probabilistic Approaches. *Hydrol. Sci. J.* **2010**, *55*, 364–376. [CrossRef]

87. Horritt, M.S.; Di Baldassarre, G.; Bates, P.D.; Brath, A. Comparing the Performance of a 2-D Finite Element and a 2-D Finite Volume Model of Floodplain Inundation Using Airborne SAR Imagery. *Hydrol. Process.* **2007**, *21*, 2745–2759. [CrossRef]

88. Lim, N.J.; Brandt, S.A. Flood Map Boundary Sensitivity Due to Combined Effects of DEM Resolution and Roughness in Relation to Model Performance. *Geomat. Nat. Hazards Risk* **2019**, *10*, 1613–1647. [CrossRef]

89. Sampson, C.C.; Smith, A.M.; Bates, P.D.; Neal, J.C.; Alfieri, L.; Freer, J.E. A High-Resolution Global Flood Hazard Model. *Water Resour. Res.* **2015**, *51*, 7358–7381. [CrossRef]

90. Shastry, A.; Durand, M.; Neal, J.; Fernández, A.; Phang, S.C.; Mohr, B.; Jung, H.C.; Kari, S.; Moritz, M.; Mark, B.G.; et al. Small-Scale Anthropogenic Changes Impact Floodplain Hydraulics: Simulating the Effects of Fish Canals on the Logone Floodplain. *J. Hydrol.* **2020**, *588*, 125035. [CrossRef]

91. Meteo. MeteoSearch (In Greek). Available online: https://meteosearch.meteo.gr/ (accessed on 8 November 2023).

92. Varlas, G.; Stefanidis, K.; Papaioannou, G.; Panagopoulos, Y.; Pytharoulis, I.; Katsafados, P.; Papadopoulos, A.; Dimitriou, E. Unravelling Precipitation Trends in Greece since 1950s Using ERA5 Climate Reanalysis Data. *Climate* **2022**, *10*, 12. [CrossRef]

93. CORINE Land Cover Database. Available online: https://land.copernicus.eu/en/products/corine-land-cover (accessed on 13 December 2023).

94. Kathimerini. Satellite images of the post-flood destructed Kineta. *Καθημερινή*. 2019. (In Greek). Available online: https://www.kathimerini.gr/society/976424/sygklonistikes-eikones-apo-doryforo-tis-fotias-stin-kineta/ (accessed on 8 November 2023).

95. UPstories. Kineta Greece after Disaster. Up Stories—YouTube. Available online: https://www.youtube.com/watch?v=EDr5sZqQMnw (accessed on 12 November 2023).